ADVANCED MATERIALS
www.advmat.de

Large Anomalous Nernst Effects at Room Temperature in Fe_3Pt Thin films

Minghang Li, Hanqi Pi, Yunchi Zhao, Ting Lin, Qinghua Zhang, Xinzhe Hu, Changmin Xiong, Zhiyong Qiu, Lichen Wang, Ying Zhang, Jianwang Cai, Wuming Liu, Jirong Sun, Fengxia Hu, Lin Gu, Hongming Weng, Quansheng Wu,* Shouguo Wang,* Yunzhong Chen,* and Baogen Shen*

Heat current in ferromagnets can generate a transverse electric voltage perpendicular to magnetization, known as anomalous Nernst effect (ANE). ANE originates intrinsically from the combination of large Berry curvature and density of states near the Fermi energy. It shows technical advantages over the conventional longitudinal Seebeck effect in converting waste heat to electricity due to its unique transverse geometry. However, materials showing giant ANE remain to be explored. Herein, a large ANE thermopower of $S_{yx} \approx 2$ μV K^{-1} at room temperature in ferromagnetic Fe_3Pt epitaxial films is reported, which also show a giant transverse thermoelectric conductivity of $\alpha_{yx} \approx 4$ A K^{-1} m^{-1} and a remarkable coercive field of 1300 Oe. The theoretical analysis reveals that the strong spin-orbit interaction in addition to the hybridization between Pt 5*d* and Fe 3*d* electrons leads to a series of distinct energy gaps and large Berry curvature in the Brillouin zone, which is the key for the large ANE. These results highlight the important roles of both Berry curvature and spin-orbit coupling in achieving large ANE at zero magnetic field, providing pathways to explore materials with giant transverse thermoelectric effect without an external magnetic field.

1. Introduction

Thermoelectric Seebeck effect (SE), the generation of a longitudinal electric voltage in materials when a temperature gradient is applied, can directly convert waste heat energy to electricity.[1–3] Nonetheless, the current generated by the SE which is parallel to the heat flow has limitations in the application of thermoelectric devices due to size constraints. In contrast, the Nernst effect, a transverse thermoelectric effect in a magnetic field that generates current perpendicular to the applied temperature gradient (**Figure 1**a), can greatly simplify module fabrication owing to the transverse geometry with good scalability.[4–6] Particularly, the anomalous Nernst effect (ANE) in hard ferromagnets can generate a transverse voltage from the applied heat flow without the need for an external magnetic field and thus has sparked much interest recently.[7]

M. Li, H. Pi, Y. Zhao, T. Lin, Q. Zhang, X. Hu, Y. Zhang, J. Cai, W. Liu, J. Sun, F. Hu, L. Gu, H. Weng, Q. Wu, Y. Chen, B. Shen
Beijing National Laboratory of Condensed Matter Physics and Institute of Physics
Chinese Academy of Sciences
Beijing 100190, China
E-mail: quansheng.wu@iphy.ac.cn; yzchen@iphy.ac.cn

M. Li, H. Pi, T. Lin, Y. Zhang, J. Cai, W. Liu, J. Sun, F. Hu, H. Weng, Q. Wu, Y. Chen, B. Shen
School of Physical Sciences
University of Chinese Academy of Sciences
Beijing 100049, China

C. Xiong
Department of Physics
Beijing Normal University
Beijing 100875, China
E-mail: cmxiong@bnu.edu.cn

Z. Qiu
School of Material Science and Engineering
Dalian University of Technology
Dalian 116024, China

L. Wang, B. Shen
Ningbo Institute of Materials Technology & Engineering
Chinese Academy of Sciences
Ningbo 315201, China

S. Wang
School of Materials Science and Engineering
Anhui University
Hefei 230601, China
E-mail: sgwang@ahu.edu.cn

B. Shen
Ganjiang Innovation Academy
Chinese Academy of Sciences
Ganzhou 341000, China

The ORCID identification number(s) for the author(s) of this article can be found under https://doi.org/10.1002/adma.202301339

DOI: 10.1002/adma.202301339

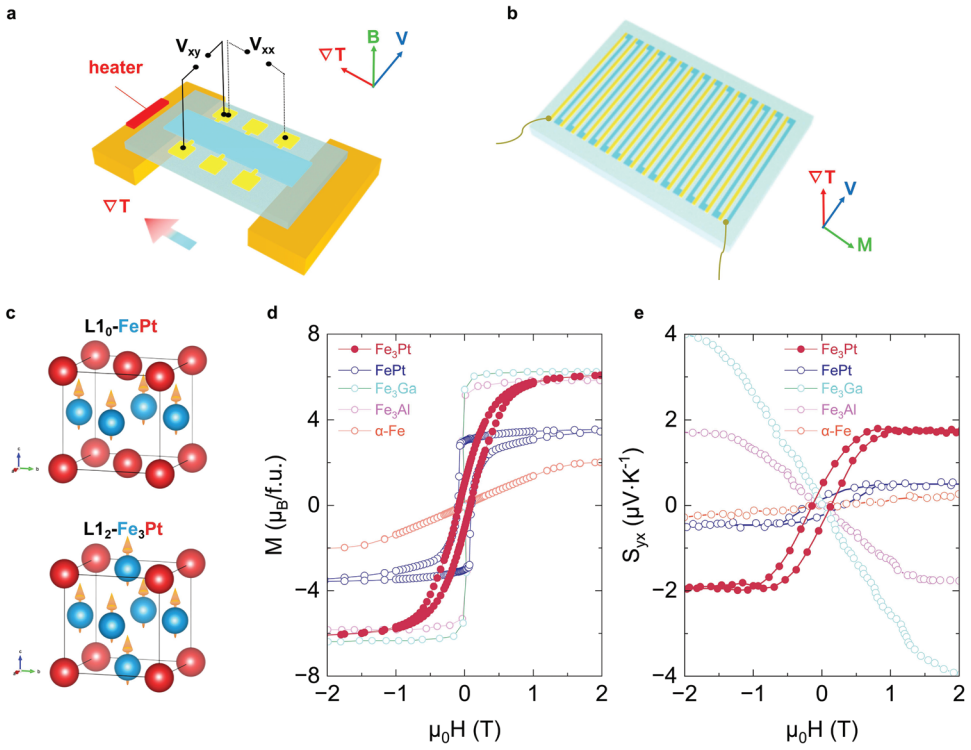

Figure 1. a) Schematic diagram of ANE (V_{xy}) and Seebeck (V_{xx}) configurations. b) Demonstration of an ANE Micro-thermoelectric conversion device. c) Crystal structures of FePt $L1_0$ ordered phase (top) and Fe_3Pt $L1_2$ ordered phase (bottom). Fe atoms are blue, Pt atoms are red. Orange arrows represent magnetic moments. d) and e) Magnetic field ($\mu_0 H$) dependence of the magnetization (M) and the ANE thermopower S_{yx}, respectively, measured at room temperature with the field up to 2 T applied perpendicular to the film plane. (The data of α-Fe,[21] Fe_3Al, and Fe_3Ga[10] are also shown for comparison, with temperature gradient applied in the film plane).

In addition, ANE devices can also be prepared into flexible structures with good extensibility (Figure 1b). Hence, the pursuit of materials with larger ANE thermopower has attracted huge interest nowadays.[7–10]

The ANE thermopower, S_{xy}, is determined by $S_{xy} = \rho_{xx}\alpha_{xy} - \rho_{yx}\alpha_{xx}$, where ρ_{xx} and ρ_{yx} are the longitudinal and Hall resistivities, and α_{xx} and α_{xy} are the diagonal and off-diagonal components of the thermoelectric conductivity tensor, respectively. The first term is the intrinsic contribution from α_{xy}, and the second term originates extrinsically from the combination of the Seebeck and Hall effects. Therefore, the anomalous Nernst response can be enhanced by either maximizing the intrinsic/extrinsic contributions or the combination of both.[11,12]

According to band theory, the intrinsic contribution of ANE thermopower, α_{xy}, at low temperatures where the thermal broadening of the Fermi energy is small, can be expressed as follows.[13,14]

$$\alpha_{xy}(\mu, T) = \frac{1}{e}\int d\varepsilon \frac{\partial f(\varepsilon)}{\partial \varepsilon}\frac{(\varepsilon-\mu)}{T}\sigma_{xy}(\varepsilon) \quad (1)$$

$$\sigma_{xy}(\varepsilon) = -\sum_n \frac{e^2}{\hbar}\int [dk]\,\Omega_{n,z}(k)\,\Theta\left(\varepsilon-\varepsilon_{n,k}\right) \quad (2)$$

where $\varepsilon_{n,k}$ and $\Omega_{n,z}(k)$ are the band energy and Berry curvature of the n-band, respectively. $\sigma_{xy}(\varepsilon)$ is the anomalous Hall conductivity at zero temperature. $f(\varepsilon)$ is the Fermi–Dirac distribution, μ is the chemical potential, $\hbar$ is the reduced Plank's constant, and $\Theta(\varepsilon - \varepsilon_{n,k})$ is the step function. This shows that the ANE originates from the Berry curvature near the Fermi surface. Therefore, designing the electronic band structure to maximize the Berry curvature near the Fermi surface is crucial to enhance the ANE, which could be beyond the conventional linear scaling law with magnetization for ferromagnets.[15] Such topologically enhanced ANE has been experimentally verified not only in ferromagnets such as Co_2MnGa,[8,16,17] Co_3Sn_2S,[7] Fe_3Al,[10] Fe_3Ga,[10] MnGa,[18] and Fe_3Sn,[19] but also in antiferromagnets such as $YbMnBi_2$,[9] Mn_3Sn,[20,21] Mn_3Ge,[22] and MnGe.[23] It is noteworthy that most of the above ferromagnets are soft ferromagnets in nature with negligible coercive fields. In other words, the ANE shrinks at low magnetic field, which also applies to antiferromagnets. Although a large Nernst thermopower of $S_{yx} \approx 3$ μV K^{-1} is achieved at zero magnetic field in magnetic Weyl-semimetal of Co_3Sn_2S[7] at 80 K, it remains rare on ferromagnetic candidates with large zero-field ANE at room temperature or above. One effective way to enhance the coercive fields in magnets is to achieve large magneto-crystalline anisotropy resulting from spin-orbit interactions, in which magnetic hysteresis results from a combination of domain dynamics and anisotropy.[24] Therefore, we studied materials based on the $L1_0$ ordered FePt, as illustrated in Figure 1c, a prototype of hard ferromagnet possessing one of the highest perpendicular magneto-crystalline anisotropy among transition metal compounds due to a large value for the Pt 5d

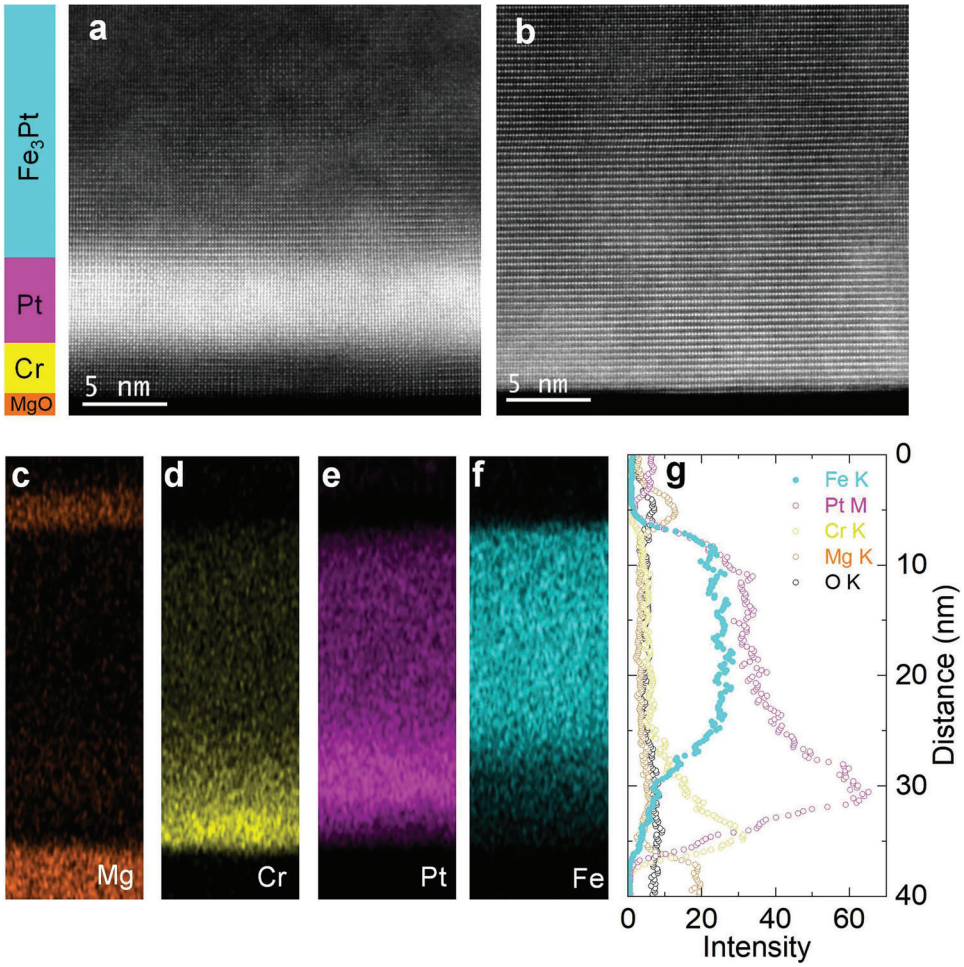

Figure 2. The atomic-resolved high-angle annular bright field (HAABF) image of the Fe_3Pt films prepared at a) 700 and b) 900 °C, respectively. c–f) EDX mappings of Mg, Cr, Pt, and Fe elements, respectively for the film grown at 700 °C. g) The line profiles for Fe_3Pt composition elements obtained from EDX mappings. Curves with different colors represent the intensity of different elements.

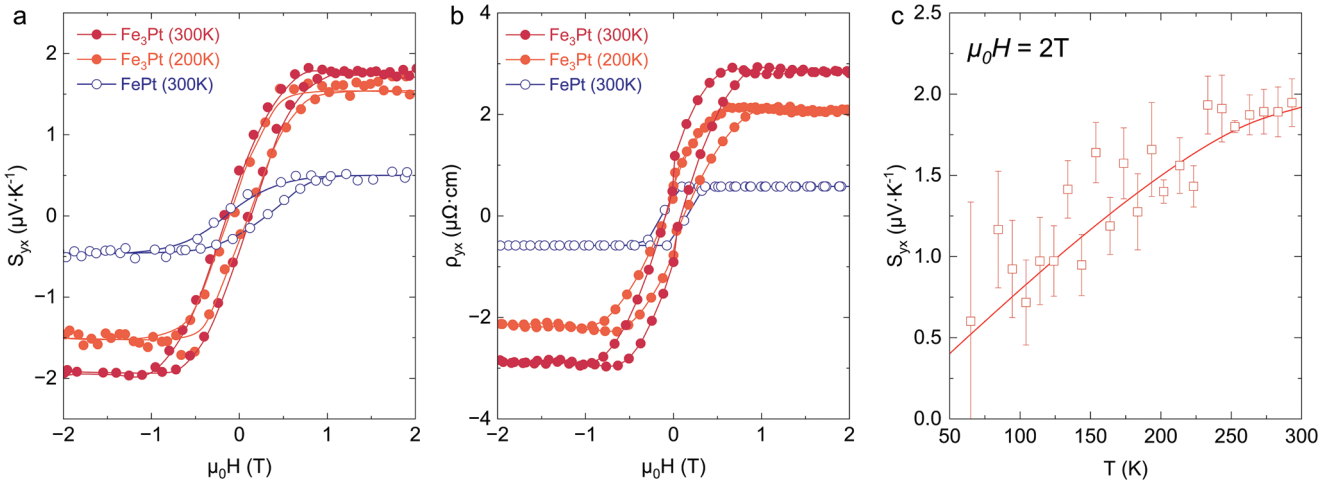

Figure 3. a,b) Magnetic field ($\mu_0 H$) dependence of the ANE thermopower, S_{yx}, and Hall resistivity, ρ_{yx}, respectively, measured in Fe_3Pt films at typical temperatures of 200 and 300 K. The data for FePt films are also shown. c) The temperature dependence of S_{yx} between 50 and 300 K under a magnetic field of 2T applied perpendicular to the film plane.

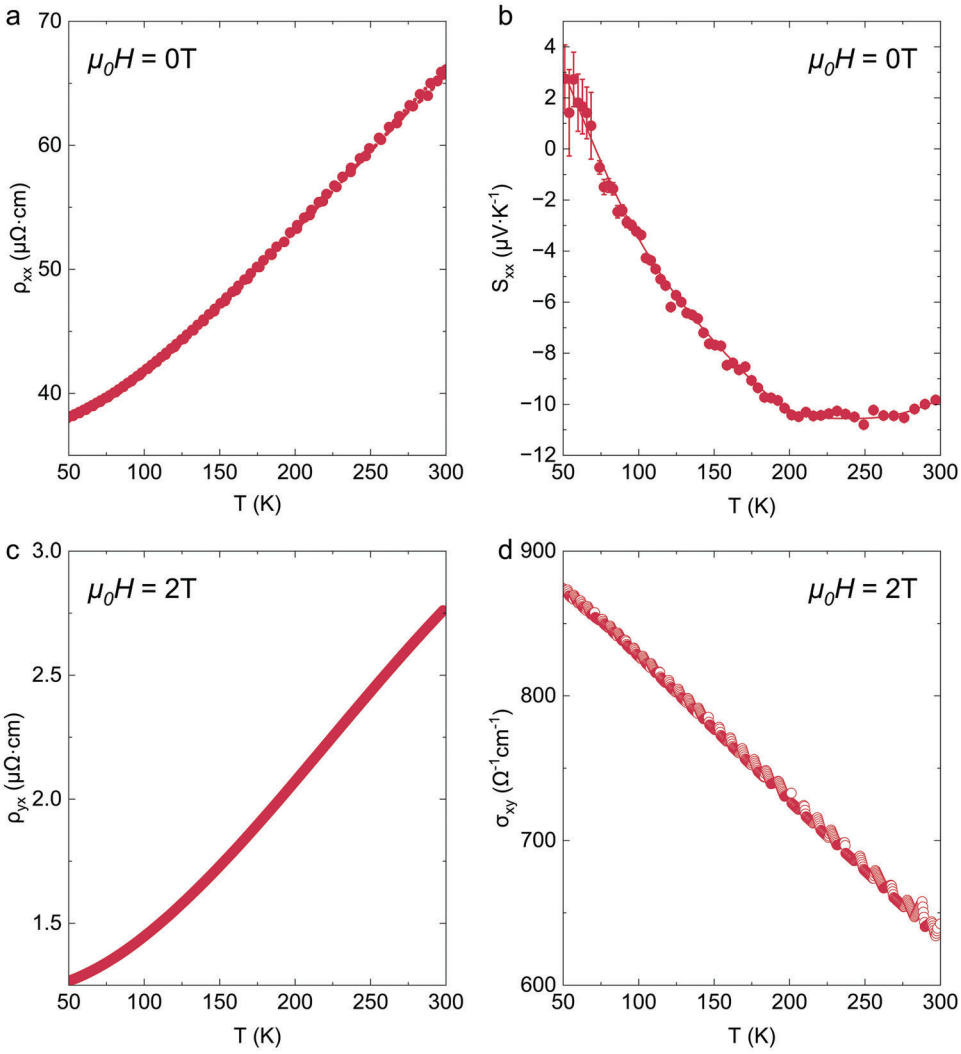

Figure 4. Temperature dependence of a) ρ_{xx}, b) S_{xx}, and c) ρ_{yx} for the Fe_3Pt films. For ρ_{yx}, a magnetic field of 2 T was applied perpendicular to the film. d) Temperature dependence of Hall conductivity (σ_{xy}).

spin-orbit interaction and strong covalent hybridization between Pt 5d and Fe 3d states.[25,26] Notably, $L1_2$ ordered Fe_3Pt, another Fe-Pt alloy which has a similar crystal structure as $L1_0$- FePt, is predicted to exhibit large $|\alpha_{yx}|$ by a high-throughput screening.[10] Nevertheless, to date, studies on ANE of Fe-Pt systems have been exclusively performed on $L1_0$-FePt[18,27,28] and Pt/Fe multilayer films[29] with moderate ANE reported ($0.5 < |S_{yx}| < 0.7$ μV K^{-1} for $L1_0$-FePt). Herein, by epitaxial growth of high-ordered Fe_3Pt films, we achieved a nontrivial quadruple enhancement in ANE thermopower to about 2 μV K^{-1} of Fe_3Pt compared to that of our FePt at room temperature. Compared to the other iron-based giant ANE compounds Fe_3Ga and Fe_3Al,[10] Fe_3Pt exhibits not only a giant transverse thermoelectric conductivity of $\alpha_{yx} \approx 4$ A K^{-1} m^{-1} but also a huge coercivity H_c of about 1300 Oe, approximately two orders of magnitude larger than that of Fe_3Al (20 Oe) and Fe_3Ga (40 Oe) films (Figure 1e). The combined electrical/thermoelectric transport measurements and density functional theory (DFT)-based calculations reveal that the large Nernst signal in Fe_3Pt originates dominantly from the intrinsic band structure in the vicinity of the Fermi energy.

2. Results and Discussion

Ordered Fe_3Pt is a cubic magnetic alloy with an $L1_2$ phase where the Pt atoms at the top and bottom of the $L1_0$-FePt unit cell are replaced by Fe atoms, as demonstrated in Figure 1c. Our epitaxial growth of the Fe_3Pt film is achieved on a Cr/Pt buffered MgO substrate. High-resolution, cross-sectional scanning transmission electron microscopy (STEM) and energy dispersive X-ray spectroscopy (EDX) were performed to determine the microstructure and interface chemistry across the heterostructure. The atomic-resolved high-angle annular bright field (HAABF) image in **Figure 2**a demonstrated the high quality of epitaxial Fe_3Pt /Pt /Cr films which were prepared at 700 °C with the single-crystalline structure of the selected area. From the analysis of the lattice parameters (Figure S2, Supporting Information),

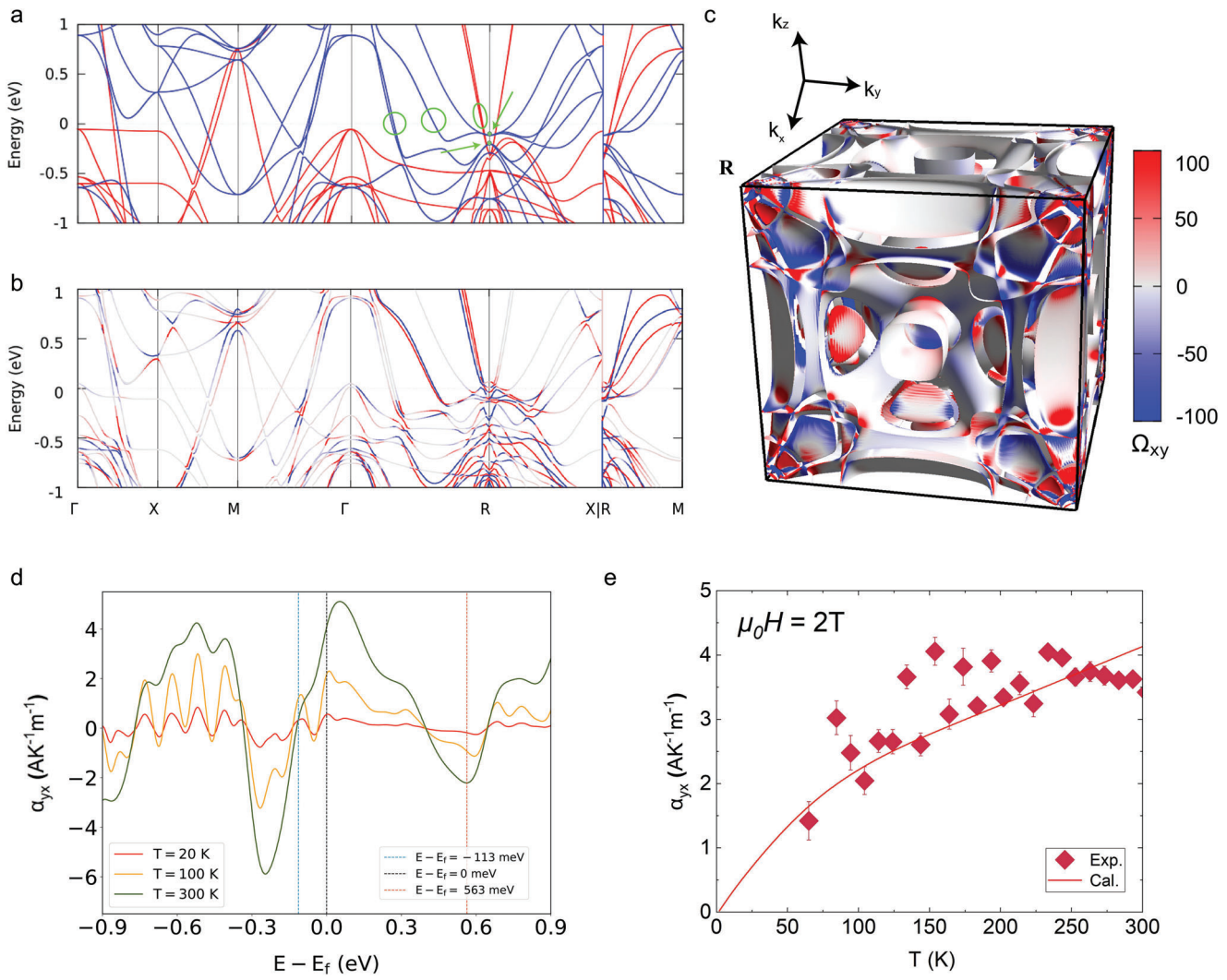

Figure 5. a) Band structure of Fe_3Pt without SOC, red/blue solid lines are the spin-majority/minority bands, respectively. The green circles/arrows denote the degenerated states on the high symmetry lines/points, respectively. b) Band structure with SOC colored by the Berry curvature $\Omega_{xy}(k)$. c) Berry curvature $\Omega_{xy}(k)$ on Fermi surfaces in the BZ. d) Calculated transverse thermoelectric conductivity, α_{yx}, as a function of the chemical potential with respect to the Fermi level at 20 K (red solid lines), 100 K (orange solid lines), and 300 K (green solid lines). The black, blue, and orange dash lines represent energy positions with respect to the Fermi energy at $\mu = E - E_F = 0$, −113, and 563 meV, respectively. e) The temperature dependence for both experimental and calculated α_{yx} with good consistency was obtained.

the brightest region represents the Pt layer. While the upper part is mostly $L1_2$-Fe_3Pt, an $L1_0$-FePt intermixing layer where Fe layers and Pt layers stacked alternately of bright and dark regions could be detected between the $L1_2$-Fe_3Pt and the Pt buffer. Subsequently, line-profile composition analysis of the sample grown at 700 °C was conducted. The resulting spatial distributions of Mg, Cr, Pt, and Fe, elements are shown by EDX mappings in Figure 2c–f, respectively, and Figure 2g summarized the evolving composition along the film thickness direction. Remarkably, sharp interfaces are observed both at the bottom Cr/MgO and the top Fe_3Pt/MgO heterostructures (Figure 2g). Within the metal layers, although a composition gradient emerges in proximity to every interface, each of the Cr, Pt, and Fe_3Pt layers exhibit spatial variations and can be well-defined. Notably, the atomic ratio of Fe:Pt for the selected Fe_3Pt and the buffered regions gives rise to 2.24 and 0.63, respectively (see in Supporting Information), indicating the intermixing $L1_0$-FePt phase is formed due to the iron downward diffusion into the Pt/Cr buffer layer. The spatial structural gradient within the metal layers arises from probably the atomic diffusion process at high temperatures and strain relaxation. For comparison, films grown at 900 °C are also shown in Figure 2b, the buffer layer is hardly detectable, which indicates significant diffusion, and the film is dominated by an $L1_0$ phase.

The epitaxial growth of Fe_3Pt thin films on MgO substrates was also confirmed by X-ray diffraction measurements (Figure S1, Supporting Information), which show a highly textured structure with both (001) and (111) diffractions at lower deposition temperatures (700 °C) with the lattice parameter calculated to be $a = b = 3.765$ Å and $c = 3.717$ Å. Notably, the diffraction peak of (001) superlattice indicates the establishment of long-range chemical ordering with the ordering parameter of S approaching 0.8,[30] further indicating the growth of highly-ordered Fe_3Pt.

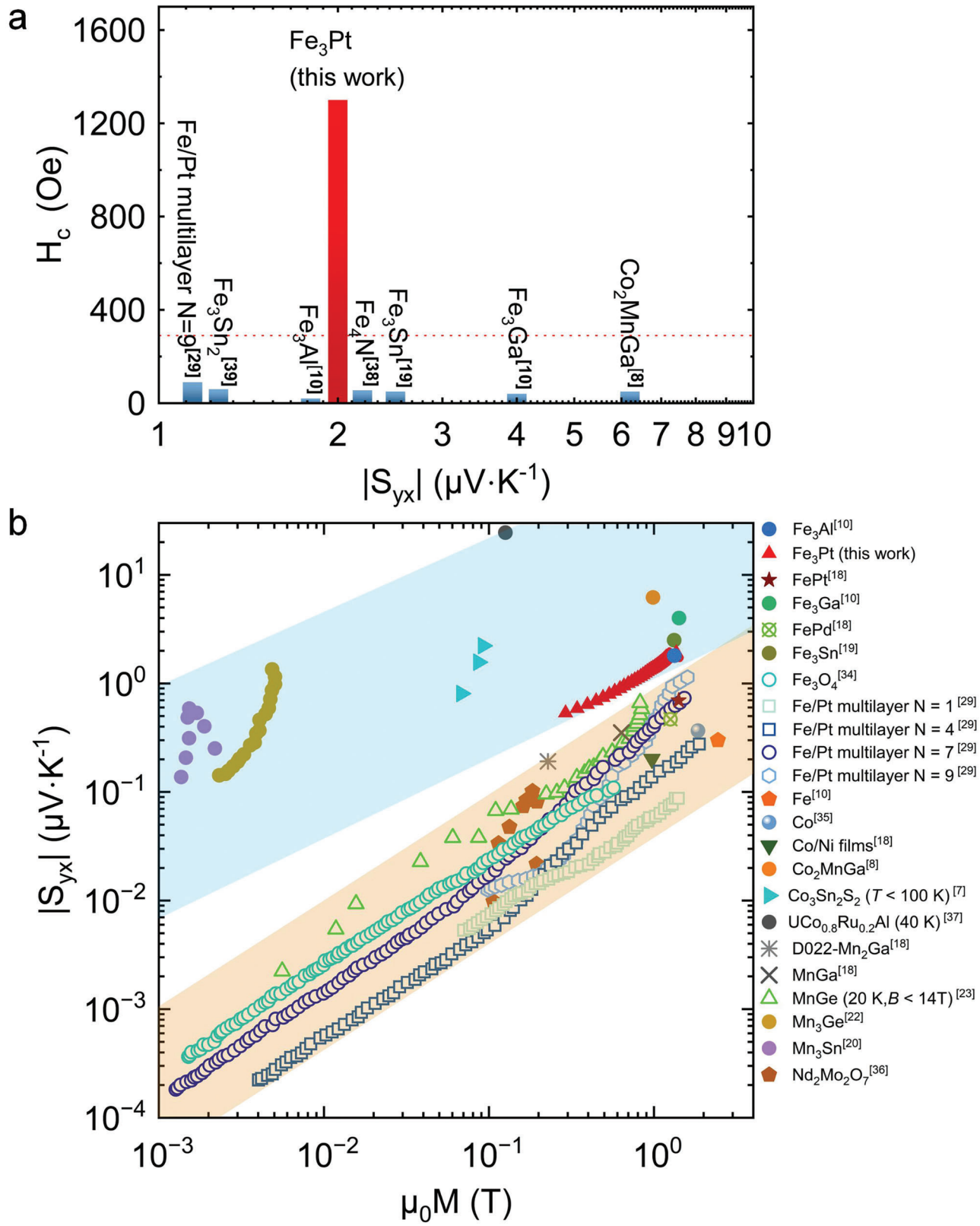

Figure 6. a) The typical coercivity, H_c, of hitherto-investigated ferromagnets with large ANE of $|S_{yx}| > 1\ \mu V\ K^{-1}$ at room temperature. The red dotted line represents the lower limit of coercivity used in magnetic stripe cards. b) Magnetization (M) scaling plot for the absolute value (S_{yx}) of ANE thermopower in both ferromagnetic and antiferromagnetic materials. The recent ANE results for conventional ferromagnetic materials and topologically-enhanced materials lie in the yellow and blue-shaded regions, respectively.

Figure 1d shows the out-of-plane magnetic hysteresis loops for Fe_3Pt at 300 K, in comparison with the data for α-Fe,[21] Fe_3Ga, and Fe_3Al.[10] Our Fe_3Pt sample exhibits a saturation magnetization of $M_S \approx 6\ \mu_B$/f.u. at magnetic fields $\mu_0 H > 1$T, comparable to that of Fe_3Al and Fe_3Ga. However, the Fe_3Pt films exhibit distinct hysteresis loops in the *M-H* curves with a considerable coercivity ($H_c \approx 1000$ Oe), which is substantially larger than that of Fe_3Al ($H_c \approx 20$ Oe) and Fe_3Ga ($H_c \approx 40$ Oe).[10] Figure 1e shows the corresponding Nernst coefficient S_{yx} as a function of magnetic field at 300 K. The clear hysteresis loop with a large coercivity of $H_c \approx 1300$ Oe in Fe_3Pt is further confirmed. Remarkably, the Fe_3Pt exhibits a $|S_{yx}| \approx 2\ \mu V\ K^{-1}$, a large ANE comparable to those of Fe_3Al ($|S_{yx}| \approx 1.8\ \mu V\ K^{-1}$) and Fe_3Ga ($|S_{yx}| \approx 4\ \mu V\ K^{-1}$),[10] which is one order of magnitude larger than α-Fe ($|S_{yx}| \approx 0.2\ \mu V\ K^{-1}$)[21] and approximately four times larger than that of FePt prepared in our work ($|S_{yx}| \approx 0.5 \mu V\ K^{-1}$).

The ANE thermopower is determined by $S_{yx} = (V_y/w)/(-\nabla_x T)$, where V_y is the ANE voltage, w is the sample width, and $\nabla_x T$ is the applied temperature gradient (as demonstrated in Figure 1a). **Figure 3**a,b show the typical magnetic field dependence of S_{yx} and ρ_{yx}, respectively, for Fe_3Pt films with a magnetic field up to 2 T. For comparison, the corresponding data of FePt film is also presented. Remarkably, at 300 K, besides the quadruple enhancement in S_{yx}, the measured values of ρ_{yx} in Fe_3Pt (2.8 μΩ cm) are about five times larger than that of FePt (0.6 μΩ cm). The ANE and anomalous Hall effect (AHE) signals have different field and temperature dependence because the ANE is determined by the Berry curvature near the Fermi surface, whereas the AHE is determined by the total integral of the Berry curvature for all occupied states in the Fermi sea.[3,7–11] Figure 3c summarized the temperature dependence of maximum S_{yx} for Fe_3Pt at 50–300 K. A moderate S_{yx} of 0.5 μV K^{-1} was observed in the Fe_3Pt film at 50 K. It exhibits a *T*-linear increase at low temperatures and reaches saturation at about 2 μV K^{-1} near room temperature, similar to the trend for Fe_3Al and Fe_3Ga.[10] Note that, at temperatures below 50 K, the low-energy phonon spectrum is dominated by quantum fluctuations, and accurate measurements are difficult to obtain because of the locked lattice structure.

In order to determine whether the large ANE is due to the intrinsic contribution from α_{xy}, or extrinsic contribution from the Seebeck/Hall effects, we studied in detail the longitudinal resistivity (ρ_{xx}), longitudinal thermoelectric power, that is, the Seebeck coefficient (S_{xx}), and the ρ_{yx}. The temperature dependence of ρ_{xx} (**Figure 4**a) exhibits typical metallic behavior as it gradually increases from 37 μΩ cm at 50 K to 66 μΩ cm at 300 K. With respect to S_{xx} as shown in Figure 4b, it decreases roughly linearly from 2.7 μV K^{-1} at 50 K to −10.5 μV K^{-1} at 200 K and becomes approximately constant in the range of 200–275 K before going up slightly to −9.6 μV K^{-1} as temperatures increase to 300 K. Moreover, the Hall resistivity ρ_{yx} at high magnetic fields where the anomalous Hall signal reaches saturation was extracted to explore the ordinary Hall effect. The negative slope indicates the dominant *n*-type charge carriers in Fe_3Pt, which is consistent with the negative sign of the Seebeck coefficient S_{xx} as shown in Figure 4b. It is notable that FePt exhibits similar temperature dependence of Seebeck coefficient as Fe_3Pt (see in Figure S8, Supporting Information) with a room temperature $S_{xx} \approx -9.2\ \mu V\ K^{-1}$ as reported previously.[27] Therefore, the Fe-Pt alloys show similar longitudinal thermoelectric power although the ANE is much enhanced in Fe_3Pt. The experimental value of Hall conductivity, $\sigma_{xy}(T)$ ($\sigma_{xy} \approx \rho_{yx}/\rho_{xx}^2$), is plotted in Figure 4d. With the increase of temperature, σ_{xy} decreases monotonically from 875 to 625 Ω^{-1} cm^{-1} in the investigated temperature range 50–300 K. Notably, the room temperature Hall conductivity ($\sigma_{xy} \approx 625\ \Omega^{-1}\ cm^{-1}$) is fairly large, comparable to the value of a 3D quantum Hall conductivity with a Chern number of unity, $\sigma_{xy} = \frac{e^2}{hc} \approx 1048\ \Omega^{-1}\ cm^{-1}$, where h is the Planck's constant and c is the lattice constant. Since $\alpha_{xx} \approx S_{xx}/\rho_{xx}$, the experimental ANE conductivity, α_{yx} ($\alpha_{yx} = -\alpha_{xy}$) is determined by the following equation as plotted in **Figure 5**e.

$$\alpha_{yx} = \frac{S_{yx}}{\rho_{xx}} - \sigma_{xy} S_{xx} \tag{3}$$

A maximum $|\alpha_{yx}|$ of 4 A K^{-1} m^{-1} is obtained at 230 K, which approaches almost saturation upon warming to 300 K. The high $|\alpha_{yx}|$ of the Fe_3Pt film ($|\alpha_{yx}^{max}| \approx 4$ A K^{-1} m^{-1}) is around five times large than that of the FePt film ($|\alpha_{yx}^{max}| \approx 0.8$ A K^{-1} m^{-1}).[28] Among the ferromagnets with large ANE, this is equal to that of Co_2MnGa ($|\alpha_{yx}^{max}| \approx 4$ AK^{-1} m^{-1})[8] and larger than the Fe_3Al film ($|\alpha_{yx}^{max}| \approx 3.8$ A K^{-1} m^{-1})[10] and $Co_3Sn_2S_2$ ($|\alpha_{yx}^{max}|| \approx 2$ A K^{-1} m^{-1}),[7] although slightly smaller than the Fe_3Ga film ($|\alpha_{yx}^{max}| \approx 5.2$ A K^{-1} m^{-1}).[10]

Based on the Mott relation, $\alpha_{yx} = \frac{-1}{e}\frac{\pi^2}{3}k_B^2 T \frac{d\sigma_{yx}(\varepsilon)}{d\varepsilon}|_{\varepsilon=\mu}$, which predicts that at low temperatures, α_{yx} is proportional to the temperature and the energy derivative of σ_{yx} at the Fermi energy. The fluctuation trend of α_{yx} is closely related to Fermi energy level positions and the gapped band structure around nodal points and nodal lines introduced by SOC.[31–33] To gain a deeper insight into the large ANE and high $|\alpha_{yx}|$ in Fe_3Pt, we performed the first-principles calculations of electronic structures and the transverse thermoelectric conductivity α_{yx} using the Kubo formula for both FePt and Fe_3Pt. The band structure of spin majority and minority without spin-orbit coupling (SOC) included for Fe_3Pt is represented in Figure 5a with red and blue solid lines, respectively. It is found that the two nearest and next-nearest energy states to the Fermi energy on R high-symmetry point are triple-degenerated states denoted by the green arrows. Besides, three energy bands crossing the Fermi energy on Γ-R high-symmetry direction are doubly degenerated, as shown by the green circles in Figure 5a. In the Supporting Information, we show that those degeneracies are not accidental but protected by symmetry. The introduction of SOC lifts the degeneracies mentioned above, leading to a series of small energy gaps and large Berry curvature as shown in Figure 5b. Because α_{yx} is determined by Berry curvature Ω_{xy} near the Fermi energy,[13,14] we calculate the $\Omega_{xy}(k)$ on the Fermi surface. As seen from Figure 5c and Figure S10, Supporting Information, $\Omega_{xy}(k)$ is distributed throughout the BZ, especially around R, which results in the large intrinsic ANE of $L1_2$-Fe_3Pt.

The calculated $\alpha_{yx}(\mu)$ as a function of chemical potential ($\mu = E - E_F$) at different temperatures is illustrated in Figure 5d. As shown by the red lines in Figure 5d and $\sigma_{yx}(\mu)$ in Figure S11a, Supporting Information, the sign of α_{yx} at 20 K is nearly determined by the slope of $\sigma_{yx}(\mu)$ at the chemical potential in accordance with the Mott relation. For instance, $\sigma_{yx}(\mu)$ at $\mu = 0$ meV

has a negative slope thus the corresponding α_{yx} is positive, while the slope of $\sigma_{yx}(\mu)$ at $\mu = 563$ meV is positive thus the corresponding α_{yx} is negative. Moreover, the $\sigma_{yx}(\mu)$ in FePt (Figure S12b, Supporting Information) has a smaller variation (≈849 S (cm·eV)$^{-1}$) at the charge neutral point compared to Fe_3Pt (≈9147 S (cm·eV)$^{-1}$), which leads to the suppression of α_{yx} in FePt (Figure S12c, Supporting Information) as predicted by the Mott relation. Besides, α_{yx} in Fe_3Pt at different chemical potentials show distinctive dependence on temperature. As represented in Figure 5d and Figure S11b, Supporting Information, the magnitude of α_{yx} with chemical potential at $\mu = 0$ meV and $\mu = 563$ meV increases as the temperature increases from 2 to 300 K. However, $|\alpha_{yx}(\mu)|$ at $\mu = -113$ meV grows firstly as temperature increases and then decreases. The calculated temperature-dependent α_{yx} at the charge neutral point ($E = E_F$) is well consistent with the experiment data as shown in Figure 5e. The dependence of α_{yx} on the temperature could be understood from the shape of $\sigma_{yx}(\mu)$ near the chemical potential, which is discussed in detail in the Supporting Information.

Finally, it is noteworthy that, up to date, among the ferromagnetic materials with large ANE with $|S_{yx}| > 1$ μV K^{-1}, only the Fe_3Pt exhibits a coercivity ($H_c \approx 1300$ Oe) larger than that of a magnetic stripe card ($H_c \approx 290$ Oe), as shown in **Figure 6**a. Furthermore, to compare the ANE in Fe_3Pt with conventional ferromagnets, we made the full logarithm plot of $|S_{yx}|$ versus the magnetization for various magnetic materials well below their Curie temperature, as shown in Figure 6b. The topologically trivial ferromagnets lie inside the blue band in the plot, with a slope of roughly one, indicating the conventional linear scaling law of the ANE signal with magnetization. Following this linear relation, the ANE thermopower for Fe_3Pt would have been 0.05–1 μV K^{-1} with the observed saturation magnetization, whereas the actual S_{yx} was about 2 μV K^{-1} at room temperature, positioning Fe_3Pt away from the conventional regime. This supports our conclusion that the large ANE in Fe_3Pt originates from the enhanced Berry curvature due to the large SOC. The large ANE thermopower and hard magnetic nature make Fe_3Pt an ideal candidate material for transverse thermoelectric devices.

3. Conclusion

To conclude, we achieved a large ANE thermopower ($|S_{yx}| \approx 2$ μV K^{-1}) at room temperature in the $L1_2$-ordered Fe_3Pt alloy film, which also possesses a large coercivity ($H_c \approx 1300$ Oe) around two orders of magnitude larger than that of Fe_3Al and Fe_3Ga. The large ANE in Fe_3Pt results from the large Berry curvature of the electronic energy states near the Fermi surface. The Fe_3Pt provides the potential for transverse thermoelectric devices without a magnetic field.

4. Experimental Section

Film Growth and Crystalline Characterization: The Fe_3Pt alloy films were deposited on MgO (001) single-crystalline substrates with by molecular beam epitaxy (MBE) with an atomic composition ratio of 75:25 at various temperatures ranging from 600 to 900 °C, which is monitored in-situ reflective high energy electron diffraction (RHEED). Before the deposition of Fe_3Pt, a 5 nm Cr/10 nm Pt buffer layer was deposited to maximize the lattice match. After deposition, a 5 nm-thick MgO layer was utilized as a capping layer to avoid oxidation. The thickness of the films was fixed at 25 nm, which is also confirmed by X-ray reflectivity (XRR). The crystalline structure was characterized by Bruker D8 X-ray diffraction (XRD) with a Cu Kα x-ray source.

Scanning Transmission Electron Microscopy (STEM): STEM measurements were conducted by a double Cs-corrected JEOL JEM-ARM200CF operated at 200 kV with a CEOS Cs corrector (CEOS GmbH, Heidelberg, Germany). The HAADF images were recorded with collection semi-angles of 90–370 mrad.

Magnetization and Magneto-Thermal Transport Measurements: The magnetic properties were measured by Quantum Design superconducting quantum interference device vibrating sample magnetometer (SQUID VSM). For magneto-thermal transport measurement, the samples were patterned into a Hall bar structure with a width of 1.0 mm and a length of 3.8 mm by using photolithography and Ar-ion milling. The AHE measurement was performed at 5 to 300 K with a perpendicular magnetic field using the Quantum Design Physics Property Measurement System (PPMS). Thermal transport properties were measured by using PPMS Thermal Transport Option (TTO) by applying a temperature gradient in the plane of samples generated by the heater shoe (Supporting Information).

The First Principles Calculation: The first-principles calculation was performed using the Vienna ab initio simulation package (VASP)[40] with the generalized gradient approximation of Perdew–Burke–Ernzerhof exchange-correlation potential.[41] The self-consistent calculation was carried out on an 11 × 11 × 11 k-mesh with an energy cutoff of 550 eV. The maximally-localized Wannier functions[42] were generated using Fe-*s/p/d* orbital and Pt-*s/d* orbital. With the tight-binding Hamiltonian constructed by the WANNIER90 package,[43] the anomalous Hall conductivity, ANE, the Fermi surface, and band structure colored with Berry curvature were calculated using the WANNIERTOOLS software package.[44]

Supporting Information

Supporting Information is available from the Wiley Online Library or from the author.

Acknowledgements

This work was supported by the Science Center of the National Natural Science Foundation of China (52088101, 12274436), the National Key Research and Development Program of China (2021YFA1400300, 2022YFA1403800), and the National Natural Science Foundation of China (52072400, 52025025, 12074334, 1218810z1), the Chinese Academy of Sciences (XDB33000000), and the Informatization Plan of the Chinese Academy of Sciences (CASWX2021SF-0102). Beijing Natural Science Foundation (Z190010).

Conflict of Interest

The authors declare no conflict of interest.

Data Availability Statement

The data that support the findings of this study are available from the corresponding author upon reasonable request.

Keywords

anomalous Nernst effect, Berry curvature, ferromagnetism, spin-orbit interactions, transverse thermoelectric effect

Received: February 11, 2023
Revised: June 4, 2023
Published online:

[1] G. J. Snyder, E. S. Toberer, *Nat. Mater.* **2008**, *7*, 105.
[2] L. E. Bell, *Science* **2008**, *321*, 1457.
[3] L. Müchler, F. Casper, B. Yan, S. Chadov, C. Felser, *Phys. Status Solidi RRL* **2013**, *7*, 91.
[4] M. Mizuguchi, S. Nakatsuji, *Sci. Technol. Adv. Mater.* **2019**, *20*, 262.
[5] Y. Sakuraba, *Scr. Mater.* **2016**, *111*, 29.
[6] W. Zhou, K. Yamamoto, A. Miura, R. Iguchi, Y. Miura, K. I. Uchida, Y. Sakuraba, *Nat. Mater.* **2021**, *20*, 463.
[7] S. N. Guin, P. Vir, Y. Zhang, N. Kumar, S. J. Watzman, C. Fu, C. Felser, *Adv. Mater.* **2019**, *31*, 1806622.
[8] A. Sakai, Y. P. Mizuta, A. A. Nugroho, R. Sihombing, T. Koretsune, M. T. Suzuki, S. Nakatsuji, *Nat. Phys.* **2018**, *14*, 1119.
[9] Y. Pan, C. Le, B. He, S. J. Watzman, M. Yao, J. Gooth, C. Felser, *Nat. Mater.* **2022**, *21*, 203.
[10] A. Sakai, S. Minami, T. Koretsune, T. Chen, T. Higo, Y. Wang, S. Nakatsuji, *Nature* **2020**, *581*, 53.
[11] M. Papaj, L. Fu, *Phys. Rev. B* **2021**, *103*, 075424.
[12] W. Zhao, Z. Liu, Z. Sun, Q. Zhang, P. Wei, X. Mu, J. Shi, *Nature* **2017**, *549*, 247.
[13] D. Xiao, Y. Yao, Z. Fang, Q. Niu, *Phys. Rev. Lett.* **2006**, *97*, 026603.
[14] G. Sharma, C. Moore, S. Saha, S. Tewari, *Phys. Rev. B* **2017**, *96*, 195119.
[15] W. L. Lee, S. Watauchi, V. L. Miller, R. J. Cava, N. P. Ong, *Phys. Rev. Lett.* **2004**, *93*, 226601.
[16] H. Reichlova, R. Schlitz, S. Beckert, P. Swekis, A. Markou, Y. C. Chen, S. T. Goennenwein, *Appl. Phys. Lett.* **2018**, *113*, 212405.
[17] S. N. Guin, K. Manna, J. Noky, S. J. Watzman, C. Fu, N. Kumar, C. Felser, *NPG Asia Mater.* **2019**, *11*, 16.
[18] K. Hasegawa, M. Mizuguchi, Y. Sakuraba, T. Kamada, T. Kojima, T. Kubota, K. Takanashi, *Appl. Phys. Lett.* **2015**, *106*, 252405.
[19] T. Chen, S. Minami, A. Sakai, Y. Wang, Z. Feng, T. Nomoto, S. Nakatsuji, *Sci. Adv.* **2022**, *8*, abk1480.
[20] M. Ikhlas, T. Tomita, T. Koretsune, M. T. Suzuki, D. Nishio-Hamane, R. Arita, S. Nakatsuji, *Nat. Phys.* **2017**, *13*, 1085.
[21] X. Li, L. Xu, L. Ding, J. Wang, M. Shen, X. Lu, K. Behnia, *Phys. Rev. Lett.* **2017**, *119*, 056601.
[22] C. Wuttke, F. Caglieris, S. Sykora, F. Scaravaggi, A. U. Wolter, K. Manna, C. Hess, *Phys. Rev. B* **2019**, *100*, 085111.
[23] Y. Shiomi, N. Kanazawa, K. Shibata, Y. Onose, Y. Tokura, *Phys. Rev. B* **2013**, *88*, 064409.
[24] J. M. D. Coey, *IEEE Trans. Magn.* **2011**, *47*, 4671.
[25] P. Ravindran, A. Kjekshus, H. Fjellvåg, P. James, L. Nordström, B. Johansson, O. Eriksson, *Phys. Rev. B* **2001**, *63*, 144409.
[26] A. Kabir, J. Hu, V. Turkowski, R. Wu, R. Camley, T. S. Rahman, *Phys. Rev. B* **2015**, *92*, 054424.
[27] M. Mizuguchi, S. Ohata, K. I. Uchida, E. Saitoh, K. Takanashi, *Appl. Phys. Express* **2012**, *5*, 093002.
[28] Z. Shi, S. J. Xu, L. Ma, S. M. Zhou, G. Y. Guo, *Phys. Rev. Applied* **2020**, *13*, 054044.
[29] K. I. Uchida, T. Kikkawa, T. Seki, T. Oyake, J. Shiomi, Z. Qiu, E. Saitoh, *Phys. Rev. B* **2015**, *92*, 094414.
[30] M. Tang, K. Shen, S. Xu, H. Yang, S. Hu, W. Lü, X. Qiu, *Adv. Mater.* **2020**, *32*, 2002607.
[31] J. Noky, Y. Zhang, J. Gooth, C. Felser, Y. Sun, *npj Comput. Mater.* **2020**, *6*, 77.
[32] B. Sohn, E. Lee, S. Y. Park, W. Kyung, J. Hwang, J. D. Denlinger, C. Kim, *Nat. Mater.* **2021**, *20*, 1643.
[33] K. Samanta, J. Noky, I. Robredo, J. Kuebler, M. G. Vergniory, C. Felser, arXiv preprint arXiv: 2212.11324, **2022**.
[34] R. Ramos, M. H. Aguirre, A. Anadón, J. Blasco, I. Lucas, K. Uchida, M. R. Ibarra, *Phys. Rev. B* **2014**, *90*, 054422.
[35] J. Weischenberg, F. Freimuth, S. Blügel, Y. Mokrousov, *Phys. Rev. B* **2013**, *87*, 060406.
[36] N. Hanasaki, K. Sano, Y. Onose, T. Ohtsuka, S. Iguchi, I. Kézsmárki, Y. Tokura, *Phys. Rev. Lett.* **2008**, *100*, 106601.
[37] T. Asaba, V. Ivanov, S. M. Thomas, S. Y. Savrasov, J. D. Thompson, E. D. Bauer, F. Ronning, *Sci. Adv.* **2021**, *7*, abf1467.
[38] S. Isogami, K. Takanashi, M. Mizuguchi, *Appl. Phys. Express* **2017**, *10*, 073005.
[39] D. Khadka, T. R. Thapaliya, S. H. Parra, J. Wen, R. Need, J. M. Kikkawa, S. X. Huang, *Phys. Rev. Mater.* **2020**, *4*, 084203.
[40] G. Kresse, J. Furthmüller, *Phys. Rev. B* **1996**, *54*, 11169.
[41] J. P. Perdew, K. Burke, M. Ernzerhof, *Phys. Rev. Lett.* **1996**, *77*, 3865.
[42] N. Marzari, D. Vanderbilt, *Phys. Rev. B* **1997**, *56*, 12847.
[43] A. A. Mostofi, J. R. Yates, G. Pizzi, Y. S. Lee, I. Souza, D. Vanderbilt, N. Marzari, *Comput. Phys. Commun.* **2014**, *185*, 2309.
[44] Q. Wu, S. Zhang, H. F. Song, M. Troyer, A. A. Soluyanov, *Comput. Phys. Commun.* **2018**, *224*, 405.